Inverse Method for Noninvasive Material Discrimination with Multienergy X-Ray Radiography

Andrew J. Gilbert,[1] Benjamin S. McDonald,[1] and Mark R. Deinert[2,*]

[1] *Pacific Northwest National Laboratory, Richland, Washington 99354, USA*

[2] *Colorado School of Mines, Golden, Colorado 80401, USA*

(Received 4 June 2022; accepted 15 August 2022; published 15 November 2022)

Active x-ray inspections have great potential for noninvasive detection of illicit materials. Dual-energy x-ray radiography, in particular, has been used to determine material composition by utilizing the energy-dependence of the x-ray attenuation coefficients. However, current implementations of this method are limited in their ability to determine the material composition of composite objects. Here we present an inverse algorithm that uses multienergy x-ray radiography data to noninvasively reconstruct the contents of a container. A critical feature of the current contribution is that material identification can be performed using conventional detectors and x-ray spectra with different endpoint energies produced by varying nothing more than the tube voltage. Adaptive regularization is used to increase the accuracy of material estimations from multienergy data sets. The utility of these methods is demonstrated with experimentally acquired radiographs obtained using a tunable x-ray source that produces spectra with endpoint energies of 100–450 keV. The object inspected is a scale model of a nuclear materials storage container composed of three-dimensional printed plastic and stainless-steel spheres inside a thin-walled steel container. Reconstructions of the steel sphere thicknesses are within a root-mean-square error of 0.37 cm.

DOI: 10.1103/PhysRevApplied.18.054043

I. INTRODUCTION

Recent arms control treaties, including New START, have resulted in the reduction of strategic nuclear weapons in the United States and Russia [1–3]. As stockpiles are further reduced under current and future arms treaties, noninvasive techniques that can accurately account for nuclear material from dismantled weapons become increasingly important. Measurements that can accurately, and noninvasively, determine material composition are essential to confirming that a weapon has been dismantled as agreed, and to aid in the nonproliferation of nuclear materials [4,5].

In general, the use of spectral information to aid in quantitative x-ray radiography has been widely applied since dual-energy body scans were introduced to help distinguish between bone and tissue, e.g., Ref. [6]. More recently, dual-energy radiography has been used in security inspections in an attempt to detect drugs, explosives, and high-atomic-numbered materials [7–9]. However, a key limitation with the dual-energy technique is that it can only determine two unknowns. Two scans are the limit in practice since models for the components of the x-ray attenuation coefficients are calculated as functions of only density and atomic number (Z). Therefore, dual-energy radiography can be used to determine an average density and atomic number for a given x-ray path length between the source and detector plane [10]. This is a significant limiting factor for detection of nuclear materials because higher-Z materials can be shielded by lower-Z materials so that the average Z is below some threshold. Dual-mode systems that use both neutron and x-ray radiography have been shown to improve material sensitivity [11,12], but at the cost of increased system complexity.

An alternate approach to dual-mode x-ray systems is to increase the amount of spectral information available for material discrimination. It was previously shown that energy-discriminating x-ray detectors can be used to differentiate between high density and nuclear materials in small, composite objects (i.e., baggage) using single scans and an inverse algorithm formulation [13]. Further, simulated dual-mode high-energy x-ray and neutron radiography have shown promise for material discrimination in large objects [14]. It has also been shown that this approach can be used in combination with tomography to verify the presence of nuclear material in warheads [15]. Here we show that an inverse algorithm can be used to discriminate several materials using standard (non-energy-discriminating) detectors and multiple x-ray spectra generated by varying the tube voltage. We demonstrate the method using a scale model of a nuclear materials storage

*mdeinert@mines.edu

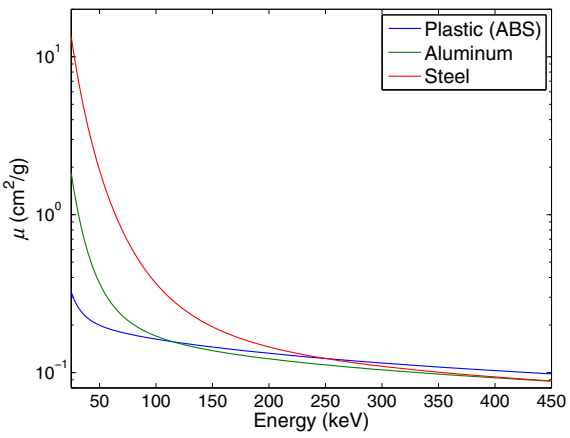

FIG. 1. Mass attenuation coefficients for a few materials of interest. The unique energy dependence of these coefficients is the basis for discriminating one material from another.

container, composed of two stainless steel spheres within a three-dimensional (3D) printed plastic mold contained within a thin-walled steel container.

II. METHODS

The interaction of an x-ray beam with an object comprised of K materials can be described using a modified form of Beer's law,

$$\Phi(\vec{\rho},E) = \Phi_0(E)\exp\left[-\sum_{k=1}^{K}\mu_k(E)\rho_k\right] + \Phi_{\text{scatter}}(E) \tag{1}$$

Here, $\Phi(\vec{\rho},E)$ [x-ray cm^{-2} keV^{-1}] is the x-ray spectral fluence at each location (x,y) on the detector plane for a given x-ray source spectrum $\Phi_0(E)$ [x-ray cm^{-2} keV^{-1}]. The energy-dependent mass attenuation coefficient for material k is μ_k [cm^2 g^{-1}], ρ_k [g cm^{-2}] is its areal density, and $\Phi_{\text{scatter}}(E)$ [x-ray cm^{-2} keV^{-1}] is the fluence from x-rays that are scattered onto the image plane. All three are also specific to each (x,y) location. The vector of areal densities for the K materials of interest is denoted by $\vec{\rho}$, which is also a function of (x,y) location. The mass attenuation coefficients can be found readily online [16] and are shown for a few materials in Fig. 1.

The radiography system response is given by:

$$\vec{d}_l(\vec{\rho}) = \frac{\mathbf{C}\,\vec{R}_l(\vec{\rho})}{\mathbf{C}'\,\vec{R}_l(\vec{0})}, \tag{2}$$

where,

$$R_l^{x,y}(\vec{\rho}) = \int_E \Phi_l^{x,y}(\vec{\rho},E)\varepsilon(E)dE. \tag{3}$$

Equation (3) describes the response of the detector to a spectral x-ray fluence. Here, both the response and the fluence are functions of the (x,y) location on the detector plane, and the values in $\Phi_l^{x,y}(\vec{\rho},E)$ are given by Eq. (1). The efficiency of the detector at energy E is denoted by $\varepsilon(E)$ [17] and the index l denotes a given x-ray source spectrum. The system response $\vec{d}_l$ is the ratio of the detector response with an object present to that with no object present, i.e., $\vec{\rho}=\vec{0}$, and $\mathbf{C}$ and $\mathbf{C}'$ are the respective convolution matrices. The ratio is taken elementwise for the vector of detector responses $\vec{R}_l(\vec{\rho})$ for all pixels of x-ray spectrum l, where the vector $\vec{\rho}$ has also been expanded to include the materials of interest at all pixels. See Supplemental Material Note 1 for additional details [18].

For a radiography system, a finite spatial resolution can be modeled with a point-spread function (PSF) that is Gaussian in shape. It is found for this system that a dual-Gaussian PSF performs better in modeling the effect when one Gaussian is narrower than the other. The narrow Gaussian likely captures the spatial resolution of the radiographic detector while the wider Gaussian captures the broadening due to flux scattered off the back wall. The finite spatial resolution is accounted for with $\mathbf{C}$ and $\mathbf{C}'$, the respective 2D convolution matrices for the object and no-object radiographs. The convolution matrices operate on the vector of detector responses $\vec{R}_l(\vec{\rho})$. Additional information is given in Supplemental Material Note 1 [18].

In practice, determining material composition from an x-ray inspection can be difficult since the material attenuation coefficients, μ, show limited uniqueness and bremsstrahlung x-ray sources have large overlapping regions in energy. Regularization [19,20] can be used to improve optimization results for such ill-posed problems, and amounts to adding additional information to the objective function to be minimized,

$$Q(\vec{\rho};\alpha,\beta,\vec{\rho}_{n-1}) = \frac{1}{2}\left\|\frac{\vec{d}(\vec{\rho})-\vec{d}_{\text{obs}}}{\sqrt{\vec{d}\,(\vec{\rho}_{n-1})}}\right\|^2 + \alpha\sum\sqrt{(\mathbf{D}_x\vec{\rho})^2+(\mathbf{D}_y\vec{\rho})^2+\beta}. \tag{4}$$

The first term on the right is the least-squares misfit. Here, $\vec{d}(\vec{\rho})$ is the forward predicted detector response for all x-ray spectra and $\vec{d}_{\text{obs}}$ is the observed response. These data vectors are a concatenation of data for all pixels at each source x-ray spectrum, i.e., $\vec{d}(\vec{\rho}) = [\vec{d}_1(\vec{\rho}),\ \vec{d}_2(\vec{\rho}),\ldots,\vec{d}_M(\vec{\rho})]$, where M is the total number of x-ray spectra that the object is scanned with. The misfit term is weighted by the square root of the elements from the previous iteration's $\vec{\rho}_{n-1}$, where n is the current iteration of the optimization, and the ratio is taken elementwise. This is done so that the variance

in the large count data does not overweight the misfit in the norm, as has been shown effective previously [13].

The second term is the total variation regularization, which includes a weighting term α that varies the strength of the regularization and the term β ensures that the function is differentiable so that analytical first and second derivatives can be found for optimization. The squares of the matrix vector product $(\mathbf{D}_x\vec{\rho})^2$ and $(\mathbf{D}_y\vec{\rho})^2$ are taken elementwise and β is also added elementwise. The value of β is set to 1. Both $\mathbf{D}_x$ and $\mathbf{D}_y$ are block Toeplitz matrices that calculate the backwards finite difference of the $\vec{\rho}$ vector in the row x and column y of the image data, respectively. The summation is over all of the respective finite difference terms. The $\mathbf{D}_x$ and $\mathbf{D}_y$ matrices are defined so that the variation across image borders or between the different materials is not taken into account in the calculation of the total variational term. The optimization is then done by solving for a set of material densities at each detector pixel that results in a best match to the observed response at that pixel and x-ray spectrum.

A Newton-type algorithm is used to optimize Eq. (4). Here, $Q(\vec{\rho};\alpha,\beta,\vec{\rho}_{n-1})$ is optimized iteratively by approximating it as a locally quadratic function at each iteration and minimizing this approximation. In order to use this method, the first derivative (gradient) and second derivative (Hessian) of $Q(\vec{\rho};\alpha,\beta,\vec{\rho}_{n-1})$, or an approximation thereof, must be found at each Newton iteration. The gradient of the misfit and regularization terms are calculated analytically. The second derivative of the misfit term is approximated with the Jacobian matrix, i.e., the Gauss-Newton algorithm [19]. This is more efficient than calculating the full Hessian and is found to perform comparably to when the full analytical Hessian matrix is used. The full Hessian is calculated for the regularization term. For all the following results, regularized or unregularized, a nonnegativity constraint is put on the solution by using the projected gradient, reduced Hessian algorithm [19]. This modification to the Newton algorithm prevents updates to $\vec{\rho}$ from moving into negative density space and projects any stray component of $\vec{\rho}$ from negative space to 0.

The regularization weighting term α is selected adaptively in the algorithm, utilizing the unbiased predictive risk estimator (UPRE), as has previously been shown effective [13]. This method requires an estimation of the noise in the image data. It is found that the noise in the weighted image data, i.e., Eq. (3), is approximately normally distributed with a standard deviation of 0.0014. This value is used for the calculation of the UPRE, where an outer loop is put on the optimization algorithm that varies α to find a minimum of the UPRE. The MATLAB function *fminbnd* is used for this outer optimization, which uses the golden search method to find an optimal $\log_{10}(\alpha)$ to a tolerance of 0.05. Optimal values of α used here range from about $10^{-7.1}$ to $10^{-6.8}$. Additional information is contained in Supplemental Material Note 2 [18].

An initial guess for $\vec{\rho}$ is set in the algorithm to the zero vector, $\vec{0}$, and a stopping criterion for the Newton iterations is set to be when the maximum change in any value of $\vec{\rho}$ is less than 10^{-4}. The algorithm is implemented in MATLAB.

A. Experimental setup and radiography

The bremsstrahlung x-ray source used for this work is a Comet MXR-451/26. It has a tungsten target at a 30° takeoff angle with 5-mm integrated beryllium filtering, a variable source spot size of 2.5 mm or 5.5 mm, and is tunable from 100 to 450 kV(peak) with a maximum current of 4.9 A. The detector is a PerkinElmer XRD-0822-AP, which has a 140-μm-thick $Gd_2O_2S:Tb$ (GOS) scintillator and a 1024 × 1024-pixel matrix of 200-μm pitch. The signal output is digitized to 16 bits and the readout electronics are shielded to reduce noise. For the purposes of the image model, Eq. (3), the bremsstrahlung spectrum $\Phi_{0,l}$ is modeled in MCNP5 [21] and ε is estimated based on the total attenuation expected in the GOS scintillator. Additional information on the radiographic setup can be found in Supplemental Material Note 3 [18].

The object inspected is a scale model of an AT400R [14] nuclear materials storage container. It is composed of two 1.91-cm-diameter stainless-steel spheres held in a plastic [acrylonitrile butadiene styrene (ABS)] cylinder, which is placed in a steel can. The plastic piece (ABS-P400, Stratasys) is made with a 3D printer and has a diameter of 10.1 cm with cavities to hold the spheres. This object is shown in Fig. 2(a), along with the experimental setup, Fig. 2(b). The radiograph of the object is shown in Fig. 3. Here, the dark current image has been subtracted and the flat-field (no object) image divided from the object image.

B. Estimation of the Φ_{scatter} term

Scattering is estimated by comparing a simulated data set using a ray-tracing attenuation data model without a scattered flux contribution to the observed data. This is similar to other work that estimated a scatter term based on the observed flux on heavily shielded image boundaries [22]. The difference between the real and simulated data is calculated for each incident spectrum and the difference is fit with a 2D second-order polynomial. Additional information on this estimation can be found in Supplemental Material Note 4 [18].

C. Error calculations

The root-mean-square error (RMSE) is used as a measure of goodness of fit of the material estimates from the algorithm to an approximation of the actual steel sphere thicknesses. The RMSE is calculated here by comparing the steel sphere thicknesses output from the inverse algorithm to a theoretical spherical profile at the same locations as the steel spheres in the radiograph. This theoretical

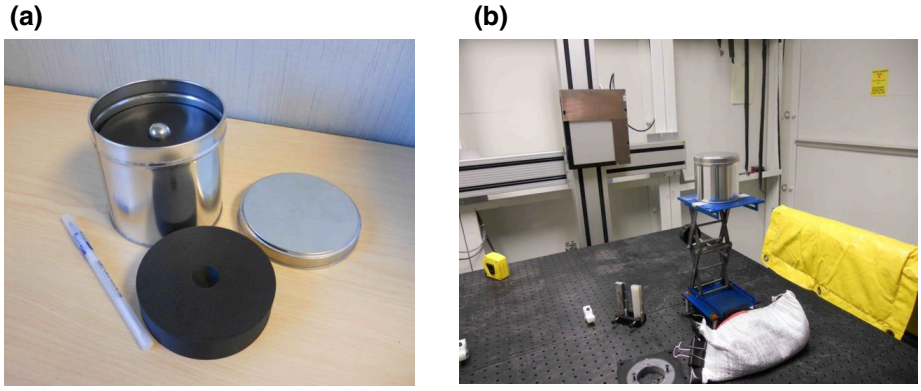

FIG. 2. Experimental system and beam floor. (a) The scale model object used in these inspections. It is composed of a thin-walled steel container with stacked, 3D-printed ABS pieces, which have two spherical cavities to set the steel spheres into. (b) The experimental setup with the object and detector visible. The source is located behind the camera, along the axis from the object to the detector.

profile is used in the absence of a ground truth for the steel sphere thicknesses. The RMSE is then the average over all steel-estimated pixels in the region of the steel spheres.

III. RESULTS

Figure 4(a) shows the results for experimentally obtained radiographs when four x-ray spectra of 150, 250, 300, and 450 keV endpoint energies are used. Results both with and without regularization are shown. The chosen basis material set is {steel, aluminum, ABS plastic}, consistent with the actual scale model composition. The regularization weighting factor α is adaptively chosen, and is found to be $10^{-7.1}$. The results with regularization show the steel spheres with high contrast, and the profile of the steel can is visible in the steel estimation, indicating submillimeter precision with these methods. Even so, the maximum steel thickness of the steel spheres is underestimated by about 0.28 cm, at 1.63 cm when it should be 1.91 cm. In contrast, the estimations without regularization are very noisy, especially in the ABS and Al results, and the steel sphere thickness is more significantly underestimated by 0.89 cm, at 1.02 cm when it should be 1.91 cm.

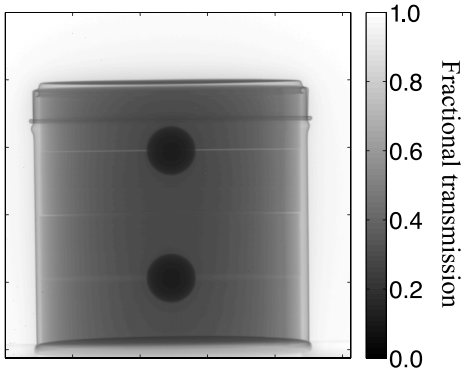

FIG. 3. An x-ray image of the scale model object used in this work. The flat-field correction is made to remove nonuniformities in the image detector response. The grayscale runs from 0 (no transmission) to 1 (complete transmission).

Figure 4(b) shows the material estimations using only two x-ray spectra with endpoint energies of 350 and 450 keV. Here, the three-basis material set is still used and regularization shows its utility in obtaining an estimated material thickness to reasonable accuracy with an otherwise underdetermined system, including sensitivity to the small steel can thickness. The value for α, picked adaptively, is $10^{-6.7}$. It might appear counterintuitive that two scans (x-ray endpoints) can be used to solve for three materials. However, regularization introduces additional information into the optimization algorithm that allows for an accurate reconstruction relative to the target material set. Here, the maximum steel sphere thickness is underestimated by about 0.54 and 0.55 cm for the regularized and unregularized cases, even though the unregularized result is considerably noisier. In this case, the RMSE better captures the difference between these results. See Table I for a summary of the experimental results.

TABLE I. The root-mean-square error (RMSE) of the estimated steel thicknesses compared with an approximation of the actual steel sphere thicknesses, for both regularized (reg.) and unregularized (unreg.) estimates. The approximation of the actual steel thicknesses is given by theoretical spherical profiles on the image plane in the same location as those in the radiograph.

Endpoint set (keV)	Reg. RMSE steel (cm)	Unreg. RMSE steel (cm)
150, 250, 300, 450	0.37	0.58
350, 450	0.45	0.66

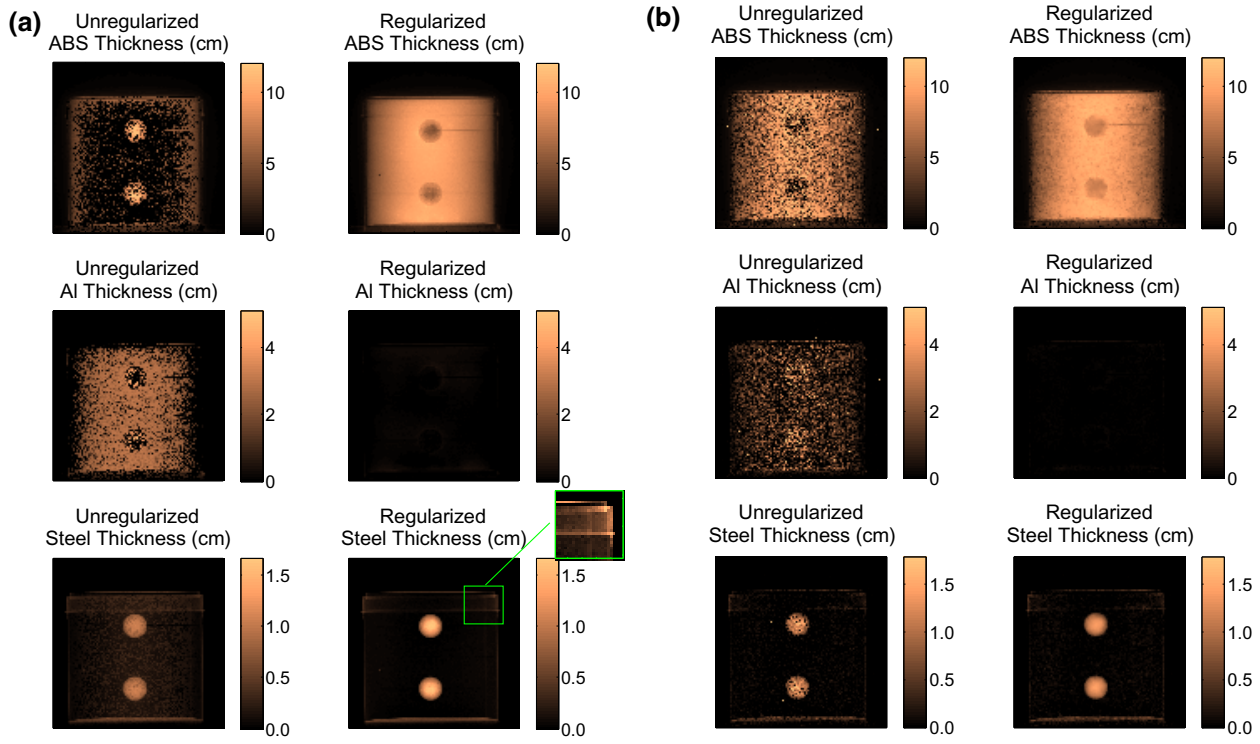

FIG. 4. Estimated material compositions from the x-ray inspections. (a) Results from a scan of 150, 250, 300, and 450 keV endpoint energies, with and without regularization. The unregularized results show significant material confusion between the ABS and Al, which is removed with the addition of regularization (there is no Al in the inspected object). The inlay from the regularized steel estimate shows good sensitivity in reconstructing the approximately 1-mm thicknesses of the steel container wall. The color scale denotes the thickness of material in centimeters. (b) Results from a scan with only the 350 and 450 keV endpoint energies show utility of the method to accurately solve an otherwise underdetermined system (three unknowns from two x-ray scans). The color scale denotes the thickness of the material in centimeters. The steel material error is summarized in Table I.

The number of materials that can be reconstructed is limited by the number of spectra, the energy dependent mass attenuation coefficients of the materials, and the regularization. The inverse approach is demonstrated here for three materials. However, reconstruction of more could be possible, particularly when the unique features of the x-ray attenuation coefficients can be observed.

In both the multi- and dual-endpoint cases, shown in Fig. 4, regularization improves the prediction of steel thickness, and eliminates the estimated presence of aluminum. However, even with regularization, the amount of steel is underpredicted by around 14%. The dominant reason for this underprediction comes from x-ray scattering from the inspected object and room onto the plane where the image of the steel spheres is generated. This has the effect of increasing the x-ray flux at these locations and making it appear as though there is less attenuation from the sphere than is really the case. As the thickness of the steel increases, this becomes more of an issue because the unattenuated flux through the spheres approaches the magnitude of the scattered flux. Both effects would be reduced with the use of an antiscatter grid.

IV. CONCLUSIONS

The results presented here show that multienergy radiography can be used in conjunction with an inverse algorithm and regularization to determine the material composition of objects using conventional x-ray detectors. The method described can be used with conventional radiographic systems and provides an important advance for detection of nuclear materials in containers and treaty verification [15,23]. Though the methods presented here are for the quantification of materials in small containers with midenergy x-ray scans, they could also be used with higher-energy inspections of larger items, such as cargo containers, trucks, etc. The algorithms would still rely on the use of a set of suspected materials, though flexibility could be built into the methods for more complex objects.

ACKNOWLEDGMENTS

This work was partially supported by the U.S. Department of Energy, National Nuclear Security Agency, Office of Defense Nuclear Non-Proliferation Research and Development. A.J.G. is supported by the Office of International Nuclear Safeguards. A portion of the research

was performed using PNNL Institutional Computing at Pacific Northwest National Laboratory. Pacific Northwest National Laboratory is operated for the U.S. Department of Energy by Battelle, under Contract No. DE-AC05-76RL01830. The external release identifier for this publication is PNNL-SA-122169.

[1] Treaty with the Union of Soviet Socialist Republics on the Reduction and Limitation of Strategic Offensive Arms (The Start Treaty) (1991).
[2] Moscow Treaty, Vol. Treaty Document 107-8 (2002).
[3] Treaty with Russia on Measures for Further Reduction and Limitation of Strategic Offensive Arms (The New Start Treaty), Vol. Treaty Document 111-5 (2010).
[4] J. Medalia, Detection of Nuclear Weapons and Materials: Science, Technologies, Observations, Detect. Nucl. Weapons Mater. 21 (2010).
[5] J. Nichol, Central Asia's New States: Political Developments and Implications for U.S. Interests, 20 (2002).
[6] R. B. Mazess, H. S. Barden, J. P. Bisek, and J. Hanson, Dual-energy x-ray absorptiometry for total-body and regional bone-mineral and soft-tissue composition, Am. J. Clin. Nutr. **51**, 1106 (1990).
[7] G. Chen, G. Bennett, and D. Perticone, Dual-energy x-ray radiography for automatic high-*Z* material detection, Appl. Accel. Res. Ind. **261**, 356 (2007).
[8] V. Moulin, V. Rebuffel, M. Antonakios, R. Sauze, and J. P. Gorius, X-Ray Imaging Modalities For Nuclear Waste Drums Inspection, in (2004).
[9] R. C. Runkle, T. A. White, E. A. Miller, J. A. Caggiano, and B. A. Collins, Photon and neutron interrogation techniques for chemical explosives detection in air cargo: A critical review, Nucl. Instrum. Methods Phys. Res., Sect. A **603**, 510 (2009).
[10] S. Ogorodnikov and V. Petrunin, Processing of interlaced images in 4–10 MeV dual energy customs system for material recognition, Phys. Rev. ST Accel. Beams **5**, 104701 (2002).
[11] S. Van Liew, X-ray and neutron interrogation of air cargo for mobile applications, Symp. Radiat. Meas. Appl. 784, 417 (2015). 2014 SORMA XV
[12] N. G. Cutmore, Y. Liu, and J. R. Tickner, in 2010 IEEE International Conference on Technologies for Homeland Security (HST) (2010), pp. 330–336.
[13] A. Gilbert, B. McDonald, S. Robinson, K. Jarman, T. White, and M. Deinert, Non-invasive material discrimination using spectral x-ray radiography, J. Appl. Phys. **115**, 154901 (2014).
[14] A. J. Gilbert, B. S. McDonald, and M. R. Deinert, Advanced algorithms for radiographic material discrimination and inspection system design, Nucl. Instrum. Methods Phys. Res., Sect. B **385**, 51 (2016).
[15] R. S. Kemp, A. Danagoulian, R. Macdonald, and J. Vavrek, Physical cryptographic verification of nuclear warheads, Proc. Natl. Acad. Sci. U. S. A. 113, 201603916 (2016).
[16] M. Chadwick, *et al.*, ENDF/B-VII.0: Next Generation Evaluated Nuclear Data Library for Nuclear Science and Technology, No. UCRL-JRNL-225066, (2006).
[17] G. F. Knoll, *Radiation Detection and Measurement*, 2nd ed. (John Wiley and Sons Inc, United States, 1989).
[18] See Supplemental Material at http://link.aps.org/supplemental/10.1103/PhysRevApplied.18.054043 for additional details.
[19] C. R. Vogel, Computational Methods for Inverse Problems, in (1987).
[20] J. M. Bardsley and A. Luttman, Total variation-penalized Poisson likelihood estimation for ill-posed problems, Adv. Comput. Math. **31**, 35 (2008).
[21] X-5 Monte Carlo Team, *MCNP—A General N-Particle Transport Code, Version 5. Volume I: Overview and Theory, Vol. 1* (Los Alamos National Laboratory, Los Alamos, NM, 2003).
[22] J. H. Siewerdsen, M. J. Daly, B. Bakhtiar, D. J. Moseley, S. Richard, H. Keller, and D. A. Jaffray, A simple, direct method for x-ray scatter estimation and correction in digital radiography and cone-beam CT, Med. Phys. **33**, 187 (2006).
[23] J. J. Hecla and A. Danagoulian, Nuclear disarmament verification via resonant phenomena, Nat. Commun. **9**, 1259 (2018).